

## Oxygen-Deficient Nickelates

## High-Temperature Structural and Electrical Characterization of Reduced Oxygen-Deficient Ruddlesden–Popper Nickelates

Ekaterina Kravchenko,<sup>[a,b]</sup> Alexandra Neagu,<sup>[c]</sup> Kiryl Zakharchuk,<sup>[a]</sup> Jekabs Grins,<sup>[c]</sup> Gunnar Svensson,<sup>[c]</sup> Vladimir Pankov,<sup>[b]</sup> and Aleksey A. Yaremchenko<sup>\*[a]</sup>

**Abstract:** High-temperature characterization of oxygen-deficient Sr-rich  $(\text{La}_{1-x}\text{Sr}_x)_2\text{NiO}_{4-\delta}$  ( $x = 0.5\text{--}0.8$ ) solid solutions under mildly reducing conditions with  $p(\text{O}_2) \approx 5 \times 10^{-5}$  atm was performed by employing structural and thermal analysis, TEM, and electrical conductivity measurements. Oxygen losses from the crystal lattice on reduction were found to result in a reversible transition from the tetragonal ( $I4/mmm$ ) to the orthorhombic ( $Immm$ ) structure and shrinkage of the crystal lattice for the compositions with  $x > 0.5$ . TEM and thermogravimetric analysis evidenced slow kinetics of the structural transition. The increase

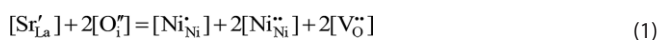
in oxygen deficiency under reducing conditions is accompanied by localization of the electronic charge carriers, a drop of the p-type electronic conductivity, and a transition from metallic-like to semiconducting behavior. The extent of changes in oxygen nonstoichiometry, unit-cell dimensions, average Ni oxidation state, electron-hole concentration, and electronic conductivity on reduction is interrelated with the strontium content. The results suggest that the electrical conductivity of  $(\text{La}_{1-x}\text{Sr}_x)_2\text{NiO}_{4-\delta}$  ceramics depends mainly on the average Ni oxidation state.

## Introduction

Rare earth nickelates  $\text{Ln}_2\text{NiO}_{4+\delta}$  ( $\text{Ln} = \text{La}, \text{Pr}, \text{Nd}$ ) belong to the family of layered perovskite-related Ruddlesden–Popper (RP) phases with the general formula  $\text{A}_{n+1}\text{B}_n\text{O}_{3n+1}$  [or  $(\text{AO})(\text{ABO}_3)_n$ ]. The  $\text{K}_2\text{NiF}_4$ -type (or RP  $n = 1$ ) structure of  $\text{Ln}_2\text{NiO}_{4+\delta}$  can be described as consisting of 2D perovskite-type  $\text{LnNiO}_3$  layers alternating with rock-salt-type  $\text{LnO}$  layers along the crystallographic  $c$  axis.<sup>[1]</sup> These phases are known to accommodate hyperstoichiometric oxygen in the form of interstitial oxygen ions located in the rock-salt  $\text{LaO}$  sheets.<sup>[1,2]</sup> Due to high oxygen diffusivity in the crystal lattice in combination with comparatively high electronic conductivity,  $\text{Ln}_2\text{NiO}_{4+\delta}$  nickelates and their derivatives attract significant attention as mixed ionic–electronic conductors (MIEC) for high-temperature electrochemical applications such as dense MIEC membranes for oxygen separation<sup>[3,4]</sup> and electrodes for solid electrolyte cells.<sup>[5–7]</sup> Oxygen-ionic transport in  $\text{Ln}_2\text{NiO}_{4+\delta}$  occurs predominantly through the migration of interstitial oxygen in rock-salt-type  $\text{LnO}$  layers, although a possible non-negligible contribution of oxygen-vacancy diffusion in perovskite layers is often

underlined.<sup>[8–10]</sup> DFT calculations predict that acceptor-type substitution by Sr in the Ln sublattice should result in a gradual transition from the formation of interstitial oxygen as dominant oxygen point defects to the generation of oxygen vacancies at high acceptor dopant contents,<sup>[11]</sup> and this also implies a change in the prevailing mechanism of ionic transport.

The  $(\text{La}_{1-x}\text{Sr}_x)_2\text{NiO}_{4-\delta}$  system is known to exhibit a wide range of solid solutions with  $\text{K}_2\text{NiF}_4$ -type structure, up to 80 atom-% of strontium in the A sublattice.<sup>[12–15]</sup> Room-temperature studies demonstrated that increasing strontium content indeed results in a gradual change from oxygen excess to stoichiometric oxygen content and even oxygen hypostoichiometry,<sup>[12–17]</sup> in agreement with theoretical calculations. In general form, the electroneutrality condition for the  $(\text{La}_{1-x}\text{Sr}_x)_2\text{NiO}_{4\pm\delta}$  series can be expressed by (using Kröger–Vink notation) [Equation (1)]:



or [Equation (2)]:

$$2x = p + 2\delta \quad (2)$$

where  $p$  is the concentration of electron holes formally residing on nickel cations (i.e.,  $\text{Ni}'_{\text{Ni}} \equiv \text{Ni}^{3+}$  and  $\text{Ni}''_{\text{Ni}} \equiv \text{Ni}^{4+}$ ) and  $\delta$  indicates oxygen deficiency (i.e.,  $\delta = [\text{V}''_{\text{O}}] - [\text{O}''_i]$ ). Thus, the concentrations of p-type electronic charge carriers and oxygen defects in  $(\text{La}_{1-x}\text{Sr}_x)_2\text{NiO}_{4\pm\delta}$  are interrelated and depend on the strontium concentration in sublattice A.

The La-rich side of the system ( $x \leq 0.5$ ,  $4 \pm \delta \geq 4$ ) was extensively studied and is well covered in the literature.<sup>[12–28]</sup> These oxides were tested for a variety of catalytic<sup>[16,29–33]</sup> and electrochemical applications; the latter include electrocatalysts for the

[a] CICECO - Aveiro Institute of Materials, Department of Materials and Ceramic Engineering, University of Aveiro, 3810-193 Aveiro, Portugal  
E-mail: ayaremchenko@ua.pt  
<http://www.ciceco.ua.pt/ayaremchenko>

[b] Department of Chemistry, Belarusian State University, Leningradskaya 14, 220006 Minsk, Belarus

[c] Department of Materials and Environmental Chemistry, Stockholm University, 106 91 Stockholm, Sweden

Supporting information and ORCID(s) for this article are available on the WWW under <https://doi.org/10.1002/ejic.201800091>.

oxygen evolution reaction in alkaline solution,<sup>[34]</sup> electrode materials for direct electrochemical reduction of NO,<sup>[35]</sup> oxygen-permeable membranes,<sup>[22,36,37]</sup> anodes for direct methanol fuel cells,<sup>[38,39]</sup> and cathodes for solid oxide fuel cells.<sup>[40–45]</sup>

At the same time, studies on the Sr-rich side of  $(\text{La}_{1-x}\text{Sr}_x)_2\text{NiO}_{4-\delta}$  system ( $x > 0.5$ ) were focused mainly on low-temperature ( $T \leq \text{r.t.}$ ) structural, electrical, and magnetic characterization,<sup>[12–15,46]</sup> available data on the high-temperature properties of these solid solutions are very limited.<sup>[22,46–48]</sup> Recently, we demonstrated that  $(\text{La}_{1-x}\text{Sr}_x)_2\text{NiO}_{4-\delta}$  ( $x = 0.5–0.8$ ) solid solutions are oxygen-deficient under oxidizing conditions at temperatures above about 500 °C.<sup>[48]</sup> The concentration of oxygen vacancies in the tetragonal  $\text{K}_2\text{NiF}_4$ -type lattice increases with increasing temperature and strontium content, and reaches  $\delta = 0.40$  for  $x = 0.8$  at 950 °C in air. The  $(\text{La}_{1-x}\text{Sr}_x)_2\text{NiO}_{4-\delta}$  ( $x = 0.5–0.8$ ) ceramics exhibit comparatively high metallic-like p-type electrical conductivity in air. Increasing oxygen deficiency was evidenced to have a positive effect on the electrochemical activity of these materials as oxygen electrodes of solid-electrolyte cells.<sup>[48]</sup> This was attributed to increasing contribution of oxygen-ionic transport to the total electrical conductivity.

Oxygen chemical-potential gradients in electrode layers under polarization may strongly affect electrical transport properties, (electro)catalytic activity, as well as kinetics and reversibility of possible redox and structural changes in electrode materials. This is caused by direct relationships between  $p(\text{O}_2)$ – $T$  conditions, oxygen content in the lattice, concentration of charge carriers, and crystal lattice symmetry. The present study continues the assessment of Sr-rich  $(\text{La}_{1-x}\text{Sr}_x)_2\text{NiO}_{4-\delta}$  ( $x = 0.5–0.8$ ) nickelates as potential cathode materials for solid oxide fuel cells<sup>[48]</sup> and is focused on the high-temperature structural and electrical properties of these phases under mildly reducing conditions equivalent to inert gas atmosphere. Such conditions can be easily induced as a result of a drop in oxygen chemical potential across the electrode layer under strong cathodic polarization. For instance, an oxygen partial pressure of  $5 \times 10^{-5}$  atm, a typical value for inert gas atmospheres, corresponds to a cathodic overpotential of approximately –190 mV at 800 °C. The characterization of reduced nickelates in this work included

variable-temperature structural studies by XRD, TEM, thermal analysis, determination of oxygen nonstoichiometry, and measurements of electrical conductivity.

## Results and Discussion

### Crystal Structure and Oxygen Nonstoichiometry of Oxidized Nickelates

As-prepared oxidized  $(\text{La}_{1-x}\text{Sr}_x)_2\text{NiO}_{4-\delta}$  ( $x = 0.5–0.8$ ) solid solutions had tetragonal  $\text{K}_2\text{NiF}_4$ -type structure (space group  $I4/mmm$ , Figure 1A). Careful inspection of the XRD patterns showed the presence of trace amounts of NiO phase impurity (tiny peaks at  $2\theta \approx 37.3$  and  $43.3^\circ$  at the background level). The intensity of impurity peaks was less than 0.9% compared to intensity of the strongest (103) reflection of the  $\text{K}_2\text{NiF}_4$ -type phase. Traces of NiO secondary phase in intermediate and Sr-rich  $(\text{La}_{1-x}\text{Sr}_x)_2\text{NiO}_{4-\delta}$  solid solutions were also mentioned in

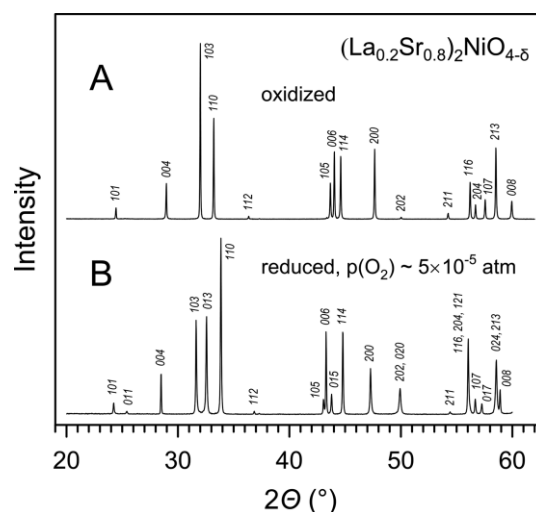


Figure 1. XRD patterns ( $\text{Cu-K}\alpha_1$  radiation) of  $(\text{La}_{0.2}\text{Sr}_{0.8})_2\text{NiO}_{4-\delta}$  ceramics: (A) oxidized (cooled in air at 2 °C/min), and (B) reduced (one heating/cooling cycle at 10 °C/min to 1000 °C at  $p(\text{O}_2) \approx 5 \times 10^{-5}$  atm). Reflections of oxidized and reduced phases are indexed in tetragonal  $I4/mmm$  and orthorhombic  $Immm$  space groups, respectively.

Table 1. Room-temperature lattice parameters of oxidized and reduced  $(\text{La}_{1-x}\text{Sr}_x)_2\text{NiO}_{4-\delta}$ .

Sample	Parameter	$x = 0.5$	$x = 0.6$	$x = 0.7$	$x = 0.8$
Oxidized	Space group	$I4/mmm$	$I4/mmm$	$I4/mmm$	$I4/mmm$
	$a/\text{Å}$	3.8271(1)	3.8293(1)	3.8261(1)	3.8182(1)
	$c/\text{Å}$	12.4562(2)	12.3676(1)	12.3310(3)	12.3446(2)
	$V/\text{Å}^3$	182.438(4)	181.353(3)	180.508(6)	179.962(4)
	$4-\delta$ <sup>[b]</sup>	4.00	4.00	4.00	3.97
	Ni oxidation state <sup>[c]</sup>	3.00	3.20	3.40	3.54
Reduced <sup>[a]</sup>	Space group	$I4/mmm$	$Immm$	$Immm$	$Immm$
	$a/\text{Å}$	3.8157(2)	3.8383(2)	3.8423(2)	3.8382(3)
	$b/\text{Å}$	–	3.7485(2)	3.7212(2)	3.6750(4)
	$c/\text{Å}$	12.5380(7)	12.5487(5)	12.5180(6)	12.5141(11)
	$V/\text{Å}^3$	182.548(14)	180.549(14)	178.981(15)	176.515(28)
	$4-\delta$	3.88	3.73	3.59	3.42
	Ni oxidation state	2.76	2.66	2.58	2.44

[a] Heating/cooling cycle at 2 °C/min to 1000 °C in inert gas flow,  $p(\text{O}_2) = 5 \times 10^{-5}$  atm. [b] Oxygen nonstoichiometry was determined by TGA. [c] Estimated assuming that oxygen ions are doubly charged.

other reports.<sup>[13,25]</sup> Room-temperature lattice parameters (Table 1) were found to be in agreement with the literature reports on this system.<sup>[12–14,20]</sup> Variable-temperature XRD studies demonstrated that all studied solid solutions preserve the tetragonal  $K_2NiF_4$ -type structure on cycling in air between room temperature and 1000 °C. The absence of phase transitions was further confirmed by differential scanning calorimetry (DSC): no thermal events could be detected in the DSC curves recorded in air in this temperature range.

Sintered  $(La_{1-x}Sr_x)_2NiO_{4-\delta}$  ceramics were comparatively porous, with relative density of 74–79 % of theoretical density (Table 2). SEM images illustrating the microstructure of sintered samples are shown in Figure S1. These ceramic samples were used for the dilatometric and electrical measurements.

Table 2. Density of as-prepared oxidized  $(La_{1-x}Sr_x)_2NiO_{4-\delta}$  ceramic samples.

$x$	Density $\rho_{\text{exptl}}$ [g cm <sup>-3</sup> ]	Relative density $\rho_{\text{exptl}}/\rho_{\text{theor}}$ [%]
0.5	4.67	74
0.6	4.69	76
0.7	4.75	79
0.8	4.38	75

All  $(La_{1-x}Sr_x)_2NiO_{4-\delta}$  ( $x = 0.5$ – $0.8$ ) lose oxygen from the crystal lattice on heating in air and are oxygen-hypostoichiometric in the high-temperature range (Figure 2A). Oxygen deficiency  $\delta$  increases with temperature and with Sr concentration in sublattice A. The onset of oxygen losses shifts to lower temperatures with increasing strontium concentration: from  $\approx 700$  °C for  $x = 0.5$  to  $\approx 300$  °C for  $x = 0.8$ . In the low-temperature range, most of the solid solutions tend to oxygen stoichiometry under

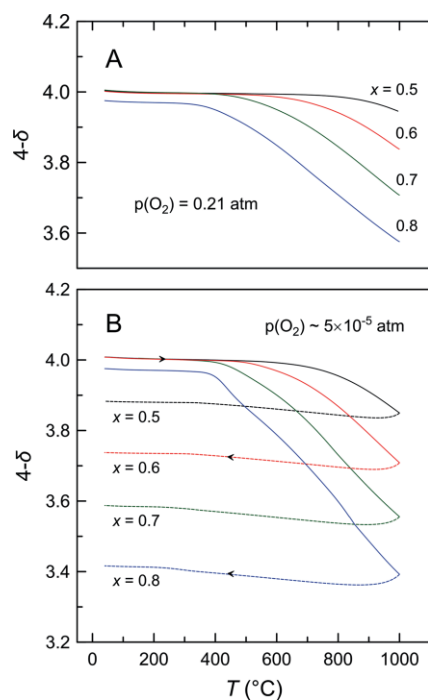


Figure 2. Variations of oxygen nonstoichiometry of  $(La_{1-x}Sr_x)_2NiO_{4-\delta}$  solid solutions: (A) on cooling in air at 2 °C/min; (B) in one reduction cycle in inert gas flow with  $p(O_2) \approx 5 \times 10^{-5}$  atm at constant heating/cooling rate of 2 °C/min.

oxidizing conditions; the only exception is the oxide with the highest strontium content, which remains slightly oxygen-deficient even at room temperature (Figure 2A and Table 1). In combination with the data reported by Nakamura et al. on La-rich compositions ( $x = 0$ – $0.2$ ),<sup>[26]</sup> these observations seem to indicate that  $(La_{1-x}Sr_x)_2NiO_{4-\delta}$  phases are not prone to switching between oxygen deficiency and oxygen excess on thermal cycling under oxidizing conditions. In other words,  $(4 \pm \delta) \geq 4$  for the compositions with a low strontium content, and  $(4 \pm \delta) \leq 4$  for heavily substituted lanthanum nickelates ( $x \geq 0.5$ ).

### Structural Changes under Mildly Reducing Conditions

Heating of air-equilibrated  $(La_{0.2}Sr_{0.8})_2NiO_{4-\delta}$  in inert gas flow with  $p(O_2) \approx 5 \times 10^{-5}$  atm reasonably results in larger oxygen losses from the lattice (Figure 3) promoted by a lower oxygen partial pressure in the gas phase. Under the applied experimental conditions, the sample apparently did not reach equilibrium state on heating to 1000 °C and continued to release oxygen during the subsequent cooling to  $\approx 900$  °C. Only minor oxygen uptake was observed in the course of cooling below 900 °C (at least partly due to a very low  $O_2$  concentration in the gas phase), and oxygen content becomes constant at temperatures  $< 250$  °C. Similar behavior was observed for other  $(La_{1-x}Sr_x)_2NiO_{4-\delta}$  solid solutions (Figure 2B). Oxygen losses on heating in inert gas flow and oxygen deficiency on subsequent cooling increased with increasing strontium content. After reduction in one heating/cooling cycle, the room-temperature oxygen content per formula unit was found to decrease from  $4 - \delta = 3.88$  for  $x = 0.5$  to  $4 - \delta = 3.42$  for  $x = 0.8$  (Table 1).

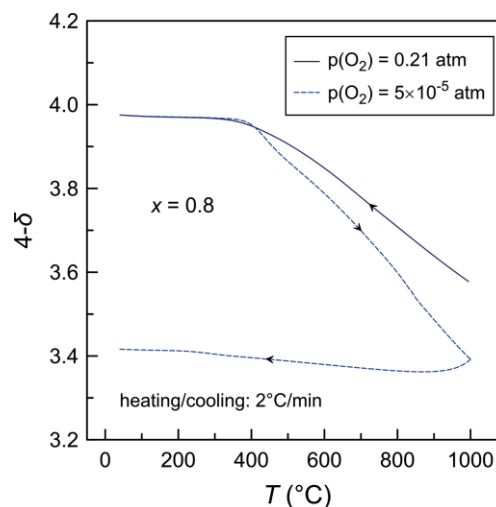


Figure 3. Variations of oxygen nonstoichiometry of  $(La_{0.2}Sr_{0.8})_2NiO_{4-\delta}$  on cooling in air and subsequent heating/cooling cycle in inert gas flow with  $p(O_2) \approx 5 \times 10^{-5}$  atm.

The results of XRD analysis indicated that  $(La_{0.5}Sr_{0.5})_2NiO_{4-\delta}$  maintains tetragonal  $I4/mmm$  structure after the reduction cycle. At the same time, the splitting of some reflections in the XRD patterns of other compositions suggested a reduction in the crystal lattice symmetry. Room-temperature XRD patterns of reduced Sr-rich  $(La_{1-x}Sr_x)_2NiO_{4-\delta}$  nickelates were indexed in orthorhombic  $Immm$  space group (Figure 1B), proposed earlier

for reduced  $(\text{Nd}_{0.2}\text{Sr}_{0.8})_2\text{NiO}_{4-\delta}$ .<sup>[49]</sup> Orthorhombic distortion is accompanied by a characteristic splitting of certain reflections [e.g. 10/ into 10/ and 01/ pairs (Figure 1B)], which becomes more evident with increasing Sr content and, therefore, oxygen deficiency (Figure 4). It was observed also that the quality of XRD data refinement in the case of  $x = 0.6$  is better if one considers a two-phase model with a fraction of tetragonal phase (Figure S2). One may assume therefore that orthorhombic and tetragonal phases coexist for this composition, at least after cooling under the conditions used in this work.

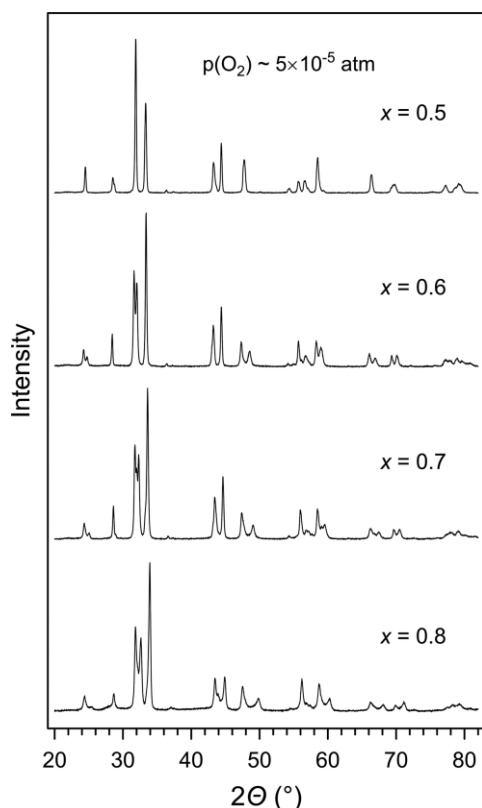


Figure 4. XRD patterns ( $\text{Cu-K}\alpha$  radiation) of  $(\text{La}_{1-x}\text{Sr}_x)_2\text{NiO}_{4-\delta}$  solid solutions after one reduction cycle in inert gas flow with  $p(\text{O}_2) \approx 5 \times 10^{-5}$  atm (see Figure 2B).

The tetragonal-to-orthorhombic structural transition implies a splitting of equatorial oxygen Wyckoff position  $4c(1/2,0,1/2)$  in the tetragonal structure (Figure 5A) into two equatorial sites  $2d(1/2,0,1/2)$  and  $2b(0,1/2,1/2)$  in the  $Immm$  subgroup (Figure 5B) with different occupation probability for these positions. Structural refinement of the neutron diffraction data for closely related  $(\text{Nd}_{0.2}\text{Sr}_{0.8})_2\text{NiO}_{3.38}$ <sup>[49]</sup> revealed that the  $2d(1/2,0,1/2)$  position is only partially occupied, whereas the other two oxygen sites do not show any detectable deviations from the stoichiometry, thus indicating the formation of an oxygen-ordered structure on reduction. The structural model implies also that Ni cations randomly adopt three different coordination states in the lattice (Figure 5B): octahedral (CN = 6), pyramidal (CN = 5), and square-planar (CN = 4). The crystal structure is closely related to that reported for La-rich  $(\text{La}_{1-x}\text{Sr}_x)_2\text{NiO}_{4-\delta}$  nickelates heavily reduced in controlled  $\text{H}_2$ -containing atmosphere and containing nickel in mixed 1+2+ oxidation state.<sup>[50–53]</sup> This

type of structure is also characteristic of orthorhombic  $\text{Sr}_2\text{CuO}_3$ ,<sup>[54,55]</sup> which adopts the same  $Immm$  space group, but with fully vacant oxygen  $2d$  Wyckoff positions and all copper ions in square-planar coordination resulting in isolated  $\text{Cu-O}$  chains (Figure 5C).

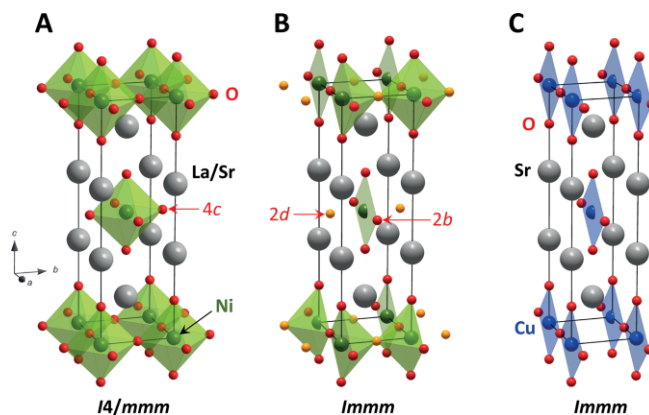


Figure 5. Schematic representation of (A) oxygen-stoichiometric tetragonal and (B) oxygen-deficient orthorhombic crystal structures of  $(\text{La}_{1-x}\text{Sr}_x)_2\text{NiO}_{4-\delta}$ ; (C) orthorhombic structure of  $\text{Sr}_2\text{CuO}_3$ .

Figure 6 shows the evolution of XRD spectra of ceramics with the highest strontium content ( $x = 0.8$ ) on heating in inert gas atmosphere with  $p(\text{O}_2) \approx 5 \times 10^{-5}$  atm. Analysis of the data indicates that the material retains tetragonal structure on heating to 700 °C. Increasing temperature is accompanied by a greater shift of the (00l) reflections to smaller angles compared to other

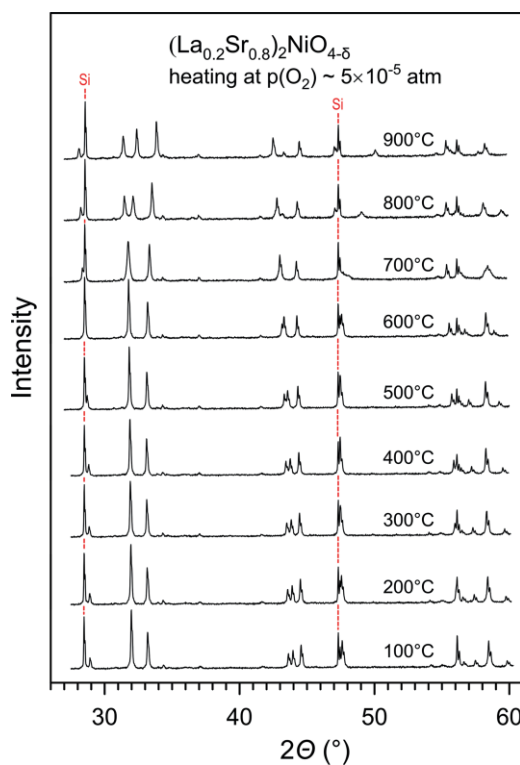


Figure 6. XRD patterns ( $\text{Cu-K}\alpha$  radiation) of oxidized  $(\text{La}_{0.2}\text{Sr}_{0.8})_2\text{NiO}_{4-\delta}$  recorded on heating from room temperature to 900 °C in inert gas flow with  $p(\text{O}_2) \approx 5 \times 10^{-5}$  atm. Dotted lines mark the reflections of the Si standard.

peaks. This is caused by a strongly anisotropic expansion of the tetragonal  $K_2NiF_4$ -type lattice on heating, namely, stronger elongation along the  $c$  axis than along the  $a$  axis, as reported for  $(Ln_{1-x}Sr_x)_2NiO_{4-\delta}$  ( $Ln = La, Nd; x = 0.5-0.8$ ) solid solutions even in air.<sup>[48,49]</sup> Splitting of certain peaks (e.g., at  $2\theta = 31.5-32.5^\circ$ ) at  $800^\circ C$  is indicative of the orthorhombic distortion; this splitting becomes even more evident on further heating to  $900^\circ C$  (Figure 6). Thus, the tetragonal-to-orthorhombic transition on heating and reduction in inert gas atmosphere occurs between  $700$  and  $800^\circ C$ , and the orthorhombic structure is maintained on cooling. This is in agreement with the DSC data recorded on heating in inert gas flow at  $10^\circ/min$ , which show the presence of a weak endothermic peak in the DSC curve of composition with  $x = 0.8$  at about  $797^\circ C$ .

The structural transition occurring on reduction at  $p(O_2) \approx 5 \times 10^{-5}$  atm was found to be reversible. The tetragonal structure and initial oxygen nonstoichiometry of  $(La_{1-x}Sr_x)_2NiO_{4-\delta}$  can be restored by annealing in air (e.g. for 5–10 h at  $1000^\circ C$ ).

### TEM Studies

Oxidized and reduced  $(La_{0.2}Sr_{0.8})_2NiO_{4-\delta}$  samples were subjected to comparative microscopic analysis. The reduced sample for this study was obtained by the heating/cooling cycle to  $1000^\circ C$  at  $10^\circ C/min$  in a flow of inert gas with  $p(O_2) \approx 5 \times 10^{-5}$  atm; this yielded a room-temperature oxygen nonstoichiometry of  $4-\delta = 3.37$ .

The representative low-magnification TEM images of oxidized and reduced  $(La_{0.2}Sr_{0.8})_2NiO_{4-\delta}$  powders are shown in Figure 7. The reduced sample shows a lamellar domain structure with domain walls parallel to  $(110)$  and  $(1\bar{1}0)$ , as marked by white arrows in Figure 7B, while the oxidized sample shows no domain contrast (Figure 7A). Moreover, for the reduced sample, a finer domain structure can be observed parallel to the  $(100)$  direction, as highlighted in the inset in Figure 7B. The lamellar domains are responsible for the significant spot splitting along  $(110)$  and  $(1\bar{1}0)$  found in the selected-area electron diffraction (SAED) patterns recorded along the  $[001]$  zone axis (ZA) (Figure 7D). Additionally, weak satellite spots can be observed around the Bragg reflections. In the case of the oxidized sample, the SAED pattern along the  $[001]$  ZA shows no splitting of the spots even at higher  $q$  values. The width of the lamellar domains is between  $10$  and  $30$  nm, while that of the finer domains is between  $3$  and  $4$  nm. The lamellar domains are actually orthorhombic twins as a result of the symmetry reduction from tetragonal  $I4/mmm$  to orthorhombic  $Immm$  with increasing oxygen deficiency.<sup>[56–58]</sup> The weak satellite spots around the Bragg reflections and the finer domain structure, observed for the reduced sample, might be associated with local vacancy ordering.

Two low-magnification images of the reduced  $(La_{0.2}Sr_{0.8})_2NiO_{4-\delta}$  sample close to  $[110]$  ZA are shown in Figure 8A. Planar defects with lighter contrast can be observed perpendicular to the  $(001)$  direction. A magnified image of the area highlighted in Figure 8A by a white square can be seen in Figure 8B. Calculations of fast Fourier transform (FFT) images of the regions marked by the white squares in Figure 8B suggest that the

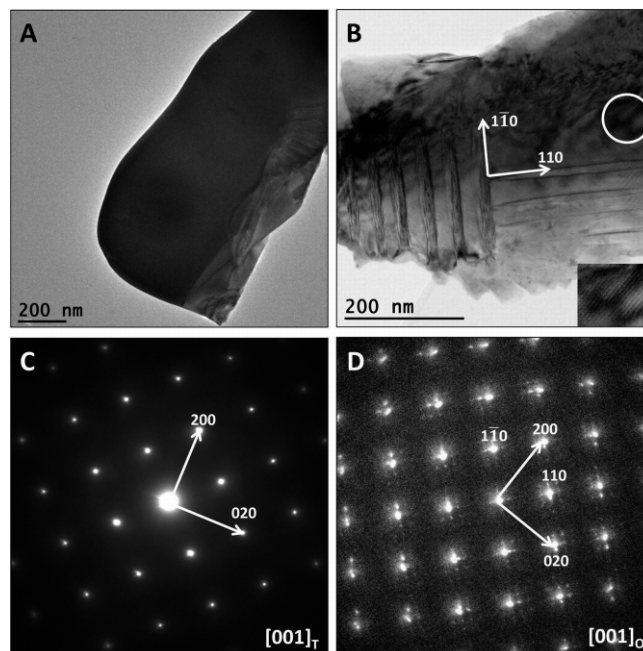


Figure 7. TEM images of (A) oxidized and (B) reduced  $(La_{0.2}Sr_{0.8})_2NiO_{4-\delta}$  powders with the corresponding SAED patterns recorded along the  $[001]$  ZA (C and D, respectively). The inset in (B) shows an enlarged view of the region marked by the white circle. T and O stand for tetragonal and orthorhombic symmetries, respectively.

planar defects are amorphous. The FFTs from regions 1 and 3 show well-defined spots, as expected for the  $[110]$  ZA, while the FFT from region 2 shows just a diffuse circle at the center. The distribution of these defects was not uniform. For the particle in Figure 8A, the defects had a width of approximately  $5$  nm. However, another particle shown in Figure S3 demonstrated a higher concentration of defects with widths varying from  $5$  to  $50$  nm.

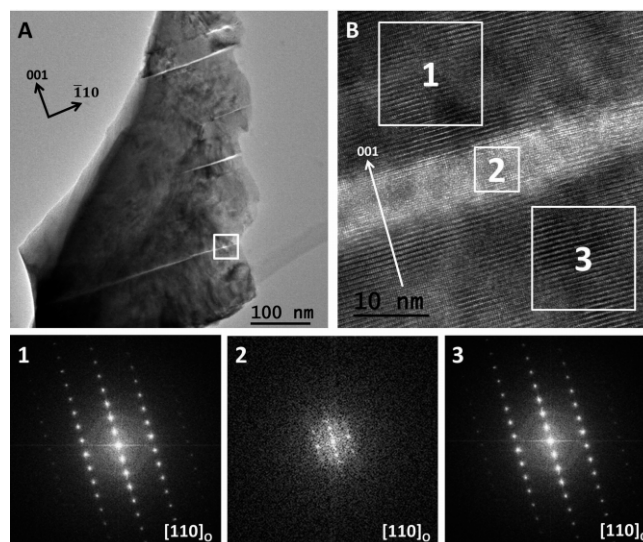


Figure 8. (A) Low-magnification image of a reduced  $(La_{0.2}Sr_{0.8})_2NiO_{4-\delta}$  particle close to  $[110]$  ZA. (B) High-resolution TEM image along the  $[110]$  ZA of the area highlighted by a white square in (A). The numbered white squares in (B) mark the areas from which the corresponding FFTs (bottom) were calculated.

The presence of planar defects in particles of reduced  $(\text{La}_{0.2}\text{Sr}_{0.8})_2\text{NiO}_{4-\delta}$  suggests that the tetragonal  $\rightarrow$  orthorhombic structural transition is not instant, occurs through an amorphous intermediate, and is not completed after one heating/cooling cycle in a gas flow with  $p(\text{O}_2) \approx 5 \times 10^{-5}$  atm. These observations are in agreement with the slow kinetics of equilibration demonstrated by thermogravimetric analysis (TGA) even at elevated temperatures. For example, Figure 9 shows the relaxation of oxygen nonstoichiometry of  $(\text{La}_{0.2}\text{Sr}_{0.8})_2\text{NiO}_{4-\delta}$  on stepwise cooling after heating to 950 °C in inert gas flow. After 10 h of equilibration at 950 °C, oxygen nonstoichiometry is still far from a constant value and continues to drop. Oxygen nonstoichiometry continues to decrease at 850 °C, but at much slower rate. Finally, the sample starts to uptake oxygen at 750 °C, although in this case the re-oxidation kinetics is also limited by a low concentration of oxygen in the gas flow.

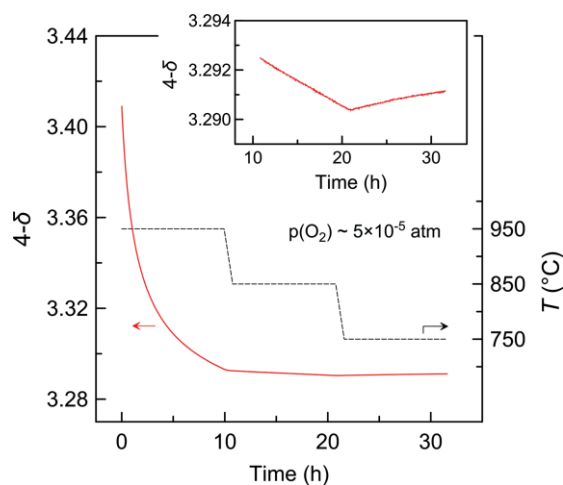


Figure 9. Relaxation of oxygen nonstoichiometry of  $(\text{La}_{0.2}\text{Sr}_{0.8})_2\text{NiO}_{4-\delta}$  on stepwise cooling in inert gas flow with  $p(\text{O}_2) \approx 5 \times 10^{-5}$  atm after heating to 950 °C at 2 °C/min in the same atmosphere. The inset shows relaxation of oxygen content at 750–850 °C with expanded vertical scale.

The HRTEM images for both oxidized and reduced  $(\text{La}_{0.2}\text{Sr}_{0.8})_2\text{NiO}_{4-\delta}$  (Figure S4A and C) reveal a well-ordered structure at the atomic scale (outside of amorphous defects). No streaking or spot splitting could be observed in the corresponding FFTs (Figure S4B and D), indicating that the crystal structure at this scale is well-ordered with one-octahedron-thick perovskite-like blocks.

### Dimensional Changes on Reduction

Figure 10 shows the dilatometric curves of oxidized  $(\text{La}_{1-x}\text{Sr}_x)_2\text{NiO}_{4-\delta}$  ceramics in one heating/cooling cycle in controlled atmosphere with  $p(\text{O}_2) \approx 5 \times 10^{-5}$  atm. In the low-temperature range, when oxygen content is constant (Figure 2B), the dilatometric curves show a linear behavior on heating, and relative elongation of the samples increases with increasing strontium content. Oxygen losses from the crystal lattice on heating above 400–600 °C (depending on composition) result in a deviation from the initial linear expansion and even shrinkage at higher temperatures for the ceramics with higher strontium content. On subsequent cooling, all the samples showed rather

smooth dilatometric behavior and overall contraction compared to the initial dimensions at room temperature (Figure 10). The extent of dimensional changes and final shrinkage of ceramics directly correlate with the strontium concentration and with the changes in oxygen nonstoichiometry in the same cycle (Figure 2B).

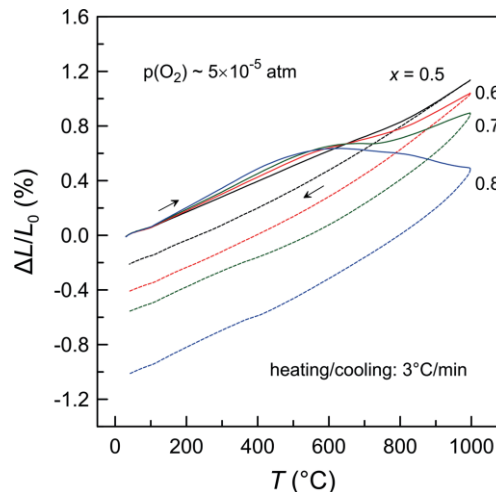


Figure 10. Dilatometric curves of oxidized  $(\text{La}_{1-x}\text{Sr}_x)_2\text{NiO}_{4-\delta}$  ceramics in one heating/cooling cycle in inert gas atmosphere.

The dilatometric data are in agreement with the room-temperature XRD results showing that the unit cells of  $(\text{La}_{1-x}\text{Sr}_x)_2\text{NiO}_{4-\delta}$  solid solutions contract after reduction and that the degree of contraction increases with increasing strontium content (Table 1 and Figure S5A). These dimensional changes can reasonably be explained by the chemical-expansion phenomenon in combination with the structural transition. Chemical expansion (or contraction) is associated with reversible changes in oxygen nonstoichiometry on temperature and redox cycling and originates from two simultaneous competing processes: (i) formation (or annihilation) of oxygen vacancies and (ii) simultaneous reduction (or oxidation) of variable-valence cations.<sup>[59,60]</sup> The formation of oxygen vacancies in the crystal lattice is supposed to induce lattice contraction due to electrostatic interactions, whereas simultaneous reduction of the variable-valence metal cations results in an increase of their ionic radii and, consequently, lattice expansion caused by steric effects. Typically, the second process has a stronger impact, and oxygen losses from the lattice on heating or decreasing  $p(\text{O}_2)$  result in the overall expansion of the crystal lattice.<sup>[59–62]</sup>

As expected, reduction of  $(\text{La}_{1-x}\text{Sr}_x)_2\text{NiO}_{4-\delta}$  solid solutions under inert gas atmosphere results in elongation along crystallographic axes  $a$  and  $c$  (Table 1). At the same time, increasing oxygen deficiency causes ordering in the oxygen sublattice, reduction of lattice symmetry, and significant contraction along the  $b$  axis. This results in overall shrinkage of the unit-cell volume (Table 1 and Figure S5A).

The only exception is the  $x = 0.5$  composition, which maintains the tetragonal structure and shows expansion along the  $c$  axis but some shrinkage along the  $a$  axis on reduction, in agreement with the data reported by Vashook et al. for the same material.<sup>[63]</sup> Furthermore, a similar trend in lattice-parameter

variations with oxygen losses was observed for tetragonal Sr-rich  $(\text{La}_{1-x}\text{Sr}_x)_2\text{NiO}_{4-\delta}$ , even on heating in air above  $\approx 700$  °C.<sup>[48]</sup> The contraction along the  $a$  axis in spite of increasing B-site cation radius can be caused by a combination of several factors. As oxygen vacancies in RP oxides form preferentially in the equatorial crystallographic positions,<sup>[64,65]</sup> the loss of electrostatic repulsion between oxide ions in  $\text{NiO}_2$  planes should favor shrinkage along the  $a$  axis. Another point is that Goldschmidt tolerance factor  $t = (r_A + r_O)/\sqrt{2}(r_B + r_O)$  for these materials is  $< 1$ ; this means that the rock-salt-type  $(\text{La,Sr})\text{O}$  layers are under tension and adjacent perovskite-like  $\text{NiO}_2$  planes are under compression. This also may work in favor of contraction in the basal plane. Finally, reduction may have different effects on the B-site cation size. On the one hand, it should increase due to decreasing oxidation state. On the other hand, reduction may be accompanied by a decrease of coordination number (at higher levels of oxygen deficiency) having an opposite effect on the ionic radius. For instance,  $r[\text{Ni}^{3+}(\text{VI,LS})] = 0.56$  Å and  $r[\text{Ni}^{2+}(\text{IV})] = 0.55$  Å.<sup>[66]</sup> Thus, a combination of different effects may rationalize some contraction in the  $ab$  plane of the  $(\text{La}_{1-x}\text{Sr}_x)_2\text{NiO}_{4-\delta}$  ( $x = 0.5$ ) tetragonal structure on reduction. Similarly to oxygen-overstoichiometric RP nickelates,<sup>[27,67,68]</sup> the variations of  $a$  and  $c$  parameters in this material compensate each other, and the unit-cell volume remains nearly unchanged on reduction (Table 1 and Figure S5A).

One should also note that the dimensional changes on heating of oxidized  $(\text{Ln}_{1-x}\text{Sr}_x)_2\text{NiO}_{4-\delta}$  ceramics in inert gas atmosphere is partly due to microcracking-related effects (Figure S6). Microcracking originates from the strongly anisotropic expansion of the tetragonal lattice of oxidized  $(\text{Ln}_{1-x}\text{Sr}_x)_2\text{NiO}_{4-\delta}$  ceramics in air partly caused by changes in the oxygen nonstoichiometry. This results in a specific dilatometric behavior on temperature cycling under oxidizing conditions, as illustrated in Figure S7 and discussed in detail elsewhere.<sup>[48,49]</sup>

Shrinkage of the crystal lattice of  $(\text{Ln}_{1-x}\text{Sr}_x)_2\text{NiO}_{4-\delta}$  nickelates on reduction-induced tetragonal  $\rightarrow$  orthorhombic transition depends on the degree of reduction (i.e., on the oxygen content in the reduced lattice). One example is shown in Figure S5B; details are also given in Table S1. Increasing oxygen deficiency was observed to be accompanied by shrinkage along the  $b$  axis, elongation along the  $c$  axis, and overall reduction of unit cell volume.

### Electrical Conductivity

Figure 11 compares electrical conductivity of oxidized and reduced  $(\text{La}_{1-x}\text{Sr}_x)_2\text{NiO}_{4-\delta}$  ceramics. All oxidized materials show metallic-like behavior in air in the studied temperature range. Quasi-2D metallic conduction in oxidized  $(\text{La}_{1-x}\text{Sr}_x)_2\text{NiO}_{4-\delta}$  nickelates is assumed to be induced by itinerant electron holes in the narrow  $\sigma_{x^2-y^2}$  band formed by delocalized  $d_{x^2-y^2}$  nickel orbitals, while  $d_{z^2}$  orbitals form a localized energy level.<sup>[12–14,18,23]</sup> Increasing temperature results in a decrease of both the electron-hole concentration  $p$  (Figure 12) and mobility  $\mu_p$  (partly due to increasing oxygen deficiency and consequently increasing scattering on oxygen vacancies), and therefore electrical conductivity. The variation of conductivity with

the strontium content under oxidizing conditions is correlated with the changes in electron-hole concentration (Figure 13A), as discussed in detail previously.<sup>[48]</sup>

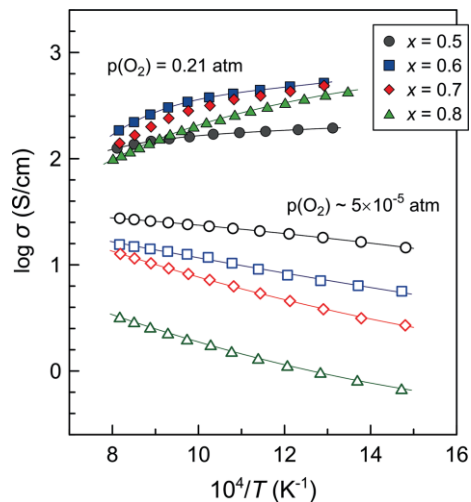


Figure 11. Temperature dependence of electrical conductivity of  $(\text{La}_{1-x}\text{Sr}_x)_2\text{NiO}_{4-\delta}$  ceramics: oxidized nickelates with tetragonal structure in air and reduced nickelates with orthorhombic lattice at  $p(\text{O}_2) \approx 5 \times 10^{-5}$  atm.

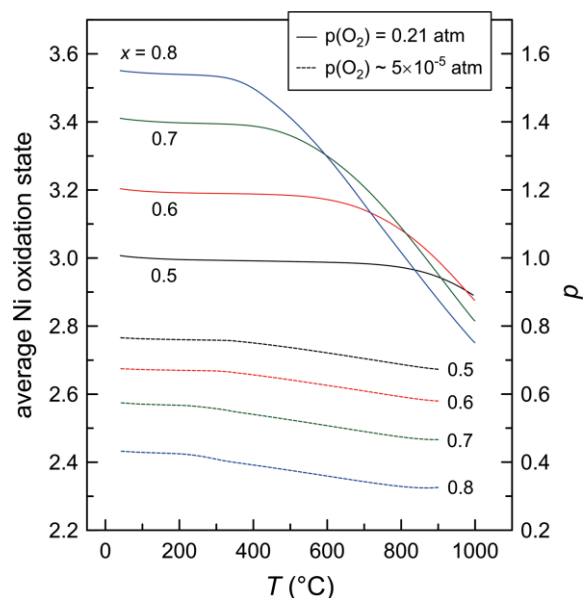


Figure 12. Temperature dependence of average nickel oxidation state and electron-hole concentration in  $(\text{La}_{1-x}\text{Sr}_x)_2\text{NiO}_{4-\delta}$  nickelates at ambient oxygen partial pressure and at  $p(\text{O}_2) \approx 5 \times 10^{-5}$  atm, as estimated from the TGA data on cooling (Figure 2) using Equation(2). The formal oxidation state of nickel cations was estimated assuming that oxygen ions are doubly-charged.

Oxygen release from the lattice on reduction in inert gas atmosphere, expressed by Equation (3),



is accompanied by a decrease of electron-hole concentration (Figure 12), decline of p-type electrical conductivity (Figure 11), and a transition from metallic to semiconducting behavior. In correlation with the changes in oxygen nonstoichiometry, the relative impact of reduction on the electrical transport increases

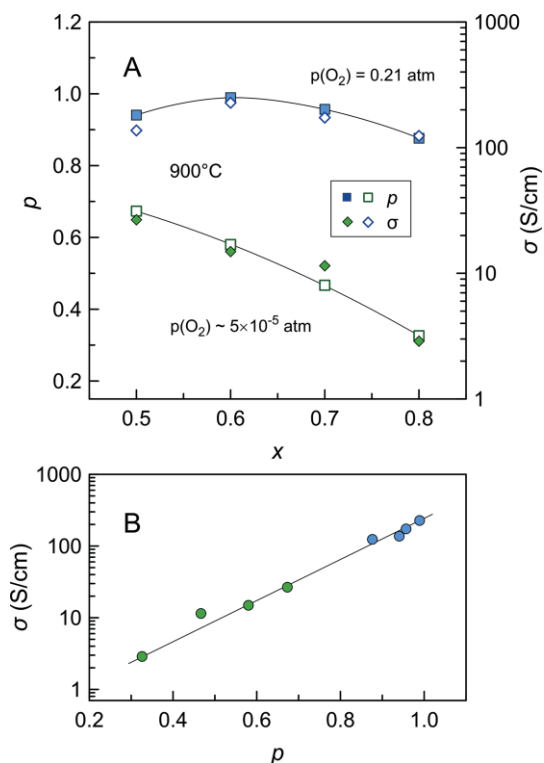


Figure 13. (A) Dependence of electron-hole concentration and electrical conductivity of oxidized and reduced  $(\text{La}_{1-x}\text{Sr}_x)_2\text{NiO}_{4-\delta}$  at 900 °C on strontium content; (B) the same values of electrical conductivity plotted versus electron-hole concentration. Blue and green symbols correspond to oxidized and reduced ceramics, respectively.

with increasing strontium content. The electrical conductivity of reduced nickelate ceramics in inert gas atmosphere decreases with increasing strontium content, while the corresponding activation energy shows the opposite trend (Table 3). As for oxidized nickelates, the variations of electron-hole concentration and electrical conductivity with  $x$  are strongly correlated (Figure 13A).

Table 3. Activation energy of electrical conductivity of reduced  $(\text{La}_{1-x}\text{Sr}_x)_2\text{NiO}_{4-\delta}$  nickelates [ $T = 400\text{--}950$  °C,  $p(\text{O}_2) \approx 5 \times 10^{-5}$  atm].<sup>[a]</sup>

$x$	$E_A$ [kJ mol <sup>-1</sup> ]
0.5	15.2 ± 0.1
0.6	21.1 ± 0.4
0.7	27.4 ± 0.6
0.8	27.4 ± 0.8

[a] Note: Activation energy was calculated using the Arrhenius model:  $\sigma = A_0/T \cdot \exp(-E_A/RT)$ ; given errors are standard errors.

Thus, a decrease in the average oxidation state of nickel cations on reduction is accompanied by localization of electronic charge carriers. Earlier, the variations of room-temperature lattice parameters with increasing  $x$  and  $\text{Ni}^{3+}$  fraction in the  $(\text{La}_{1-x}\text{Sr}_x)_2\text{NiO}_{4-\delta}$  series were interpreted as a change of electronic configuration of Ni cations and a charge redistribution between localized  $d_{z^2}$  and delocalized  $d_{x^2-y^2}$  orbitals, which eventually induce metallic-like conductivity in the low-temperature range.<sup>[12,14,18,23]</sup> Increasing oxygen deficiency on reduction is also expected to contribute to electron-hole localization by

weakening  $\text{Ni}^{n+}-\text{O}^{2-}-\text{Ni}^{n+}$  interactions or breaking nickel-oxygen bonds. Detailed studies on oxygen nonstoichiometry, electrical conductivity, and Seebeck coefficients of related  $(\text{La}_{1-x}\text{Sr}_x)_2\text{CuO}_{4-\delta}$  series demonstrated that the high-temperature electrical properties of these solid solutions are determined only by the average oxidation state of copper cations (i.e., by the concentration of electron holes).<sup>[69]</sup> It was concluded that the conduction mechanism changes continuously from hopping conduction to degenerate band conduction at an average Cu oxidation state of about 2.05+.<sup>[69]</sup> A similar situation is possibly true for the  $(\text{La}_{1-x}\text{Sr}_x)_2\text{NiO}_{4-\delta}$  system as well, although the change of the conduction mechanism occurs at higher oxidation state of nickel cations. Interestingly, if plotted together, the conductivity values for the entire range of studied  $(\text{La}_{1-x}\text{Sr}_x)_2\text{NiO}_{4-\delta}$  compositions, reduced and oxidized, seem to follow a common exponential dependence on electron-hole concentration under isothermal conditions (Figure 13B); some scattering is probably due to microstructural effects [porosity and microcracking (Table 2 and Figures S1 and S6)]. Although tetragonal-to-orthorhombic transition itself does not seem to affect the electrical transport properties to a noticeable extent, progressive ordering of oxygen vacancies in the orthorhombic lattice on further reduction should eventually lead to a transition to 1D electronic transport, as expected for  $\text{Sr}_2\text{MO}_3$  ( $M = \text{Cu, Ni, Co}$ ).<sup>[70,71]</sup>

Another comment is that the values of electrical conductivity measured under reducing conditions correspond to nearly constant oxygen content in the nickelate lattice. Long-term relaxation of electrical conductivity was noticed in the course of isothermal measurements at 850 and 750 °C after reduction at 1000 °C (Figure S8). This long-term relaxation implies a tendency of  $(\text{La}_{1-x}\text{Sr}_x)_2\text{NiO}_{4-\delta}$  ceramics to partial re-oxidation on cooling, even in inert gas atmosphere, in agreement with the thermogravimetric data (Figure 9). The oxygen uptake is kinetically limited, apparently due to the slow structural transition and very low oxygen content in the gas flow. These observations, however, do not affect the conclusion about the temperature-activated electrical transport in reduced nickelates.

## Conclusions

Oxygen losses from the crystal lattice of  $\text{K}_2\text{NiF}_4$ -type  $(\text{La}_{1-x}\text{Sr}_x)_2\text{NiO}_{4-\delta}$  ( $x = 0.5\text{--}0.8$ ) solid solutions on reduction in inert gas atmosphere with  $p(\text{O}_2) \approx 5 \times 10^{-5}$  atm result in a reversible transition from tetragonal to orthorhombic structure and shrinkage of the crystal lattice for compositions with  $x > 0.5$ . TEM and TGA evidenced slow kinetics of the structural transition. Increasing oxygen deficiency under reducing conditions is accompanied by the localization of electronic charge carriers, a drop of the p-type electronic conductivity, and a transition from metallic to semiconducting behavior. The extent of changes in oxygen nonstoichiometry, unit-cell dimensions, average Ni oxidation state (i.e. electron-hole concentration), and electrical conductivity on reduction correlates with the strontium content. The electrical conductivity of  $(\text{La}_{1-x}\text{Sr}_x)_2\text{NiO}_{4-\delta}$  seems to depend mainly on the average Ni oxidation state rather than strontium concentration or lattice symmetry.

## Experimental Section

(La<sub>1-x</sub>Sr<sub>x</sub>)<sub>2</sub>NiO<sub>4-δ</sub> ( $x = 0.5, 0.6, 0.7,$  and  $0.8$ ) ceramics were prepared by the Pechini method. The calculated amounts of La<sub>2</sub>O<sub>3</sub> (Alfa Aesar, 99.9 % purity), predried in air at 1000 °C to remove adsorbates, Sr(NO<sub>3</sub>)<sub>2</sub> (Sigma Aldrich, 99 % purity), and Ni(NO<sub>3</sub>)<sub>2</sub>·6H<sub>2</sub>O (Sigma Aldrich, 98 % purity) were dissolved in the minimal volume of 1:1 mixture of 6 M nitric acid and distilled water. Citric acid and ethylene glycol were added to the solution in a large excess (4 and 10 mol, respectively, per mole of target oxide). The prepared solutions were slowly heated to 120 °C to obtain viscous gels, which were decomposed by further heating to 350 °C and maintaining this temperature for 10 h. The products were calcined at 600–750 °C for 12 h in air to remove organic residues. The precursor powders were subsequently pelletized and calcined at 1150–1200 °C (15–30 h) under flowing oxygen with frequent regrinding until no further changes could be detected by XRD. Finally, the powders were compacted uniaxially at about 40 MPa and sintered under flowing oxygen at 1250 °C for 5 h.

Sintered ceramic samples were cut into rectangular bars and polished for the dilatometric and electrical measurements. The experimental density was calculated from the mass and geometric dimensions of the samples. Powdered samples for the structural studies and thermal analysis were prepared by grinding the sintered ceramics in a mortar.

Room-temperature XRD patterns were collected with PANalytical X'Pert Alpha-1 (Cu-K<sub>α1</sub> radiation) and Rigaku D/MAX-B (Cu-K<sub>α</sub> radiation) diffractometers. Variable-temperature XRD studies were performed in air and in inert gas atmosphere by employing a PANalytical X'Pert PRO MRD instrument (Cu-K<sub>α</sub> radiation) equipped with an Anton Parr XRK900 reaction chamber. The patterns were recorded between room temperature and 900 °C in 100 °C steps with a heating rate of 5 °C/min between the steps and equilibration for 10 min at each step before data acquisition. Rietveld refinement of XRD data was done with Fullprof software.

TEM studies were performed with a JEOL JEM-2100F microscope (C<sub>s</sub> = 0.5 mm, point resolution 1.9 Å) operated at room temperature with an accelerating voltage of 200 kV. The TEM samples were prepared by crushing the dried powders in an agate mortar followed by dispersion in ethanol. One droplet of this suspension was transferred to a copper grid coated with holey-carbon film.

Dilatometric studies were conducted in flowing air and argon atmospheres at 25–1000 °C with heating/cooling rate of 3 °C/min using a vertical Linseis L70/2001 instrument. Differential scanning calorimetry (DSC) was performed at 25–1000 °C in flowing N<sub>2</sub> with heating/cooling rate of 10 °C/min using a Netzsch STA 449 F3 analyzer. Thermogravimetric analysis (TGA, Setaram SetSys 16/18 instrument, sensitivity 0.4 µg, initial sample weight ≈ 0.5 g) was carried out on powdered samples in flowing air, argon, or 10 % H<sub>2</sub>–90 % N<sub>2</sub> mixture at 25–1000 °C with a constant heating/cooling rate. In the course of TGA studies, each dataset included equilibration of the sample with air at 950 °C. The absolute oxygen content in this reference state (air, 950 °C) was determined by TGA through in situ reduction to metallic Ni, coexisting with SrO and La<sub>2</sub>O<sub>3</sub>, in a flowing dry 10 %H<sub>2</sub>–90 %N<sub>2</sub> mixture at 950–1100 °C. Electrical conductivity  $\sigma$  was measured by the four-probe dc method as function of temperature in air and in inert gas (Ar) atmospheres at 500–1000 °C. In all cases, oxygen partial pressure in a gas flow was monitored with an yttria-stabilized zirconia solid-electrolyte sensor. Representative  $p(\text{O}_2)$  values in an inert gas (argon or nitrogen) flow corresponded to about  $5 \times 10^{-5}$  atm.

## Acknowledgments

This work was supported by the FCT, Portugal [project IF/01072/2013/CP1162/CT0001 and project CICECO-Aveiro Institute of Materials POCI-01-0145-FEDER-007679 (FCT ref. UID/CTM/50011/2013), financed by national funds through the FCT/MEC and when appropriate co-financed by FEDER under the PT2020 Partnership Agreement]. E. K. would like to acknowledge the doctoral grant by the Belarusian State University and the Visby Programme scholarship by the Swedish Institute. The Knut and Alice Wallenberg Foundation is acknowledged for funding the electron microscopy facilities at Stockholm University.

**Keywords:** Layered compounds · Nonstoichiometric compounds · Mixed-valent compounds · Nickelates · Solid-state structures · Conducting materials

- [1] M. Greenblatt, *Curr. Opin. Colloid Solid State Mater. Sci.* **1997**, *2*, 174–183.
- [2] J. D. Jorgensen, B. Dabrowski, S. Pei, D. R. Richards, D. G. Hinks, *Phys. Rev. B* **1989**, *40*, 2187–2199.
- [3] D. C. Zhu, X. Y. Xu, S. J. Feng, W. Liu, C. S. Chen, *Catal. Today* **2003**, *82*, 151–156.
- [4] A. L. Shaula, E. N. Naumovich, A. P. Viskup, V. V. Pankov, A. V. Kovalevsky, V. V. Kharton, *Solid State Ionics* **2009**, *180*, 812–816.
- [5] G. Amow, S. J. Skinner, *J. Solid State Electrochem.* **2006**, *10*, 538–546.
- [6] H. Zhao, Q. Li, L. P. Sun, *Sci. China Chem.* **2011**, *54*, 898–910.
- [7] T. Ogier, F. Mauvy, J. M. Bassat, J. Laurencin, J. Mougouin, J. C. Grenier, *Int. J. Hydrogen Energy* **2015**, *40*, 15885–15892.
- [8] A. R. Cleave, J. A. Kilner, S. J. Skinner, S. T. Murphy, R. W. Grimes, *Solid State Ionics* **2008**, *179*, 823–826.
- [9] E. N. Naumovich, V. V. Kharton, *THEOCHEM* **2010**, *946*, 57–64.
- [10] D. Lee, H. N. Lee, *Materials* **2017**, *10*, 368.
- [11] W. Xie, Y. L. Lee, Y. Shao-Horn, D. Morgan, *J. Phys. Chem. Lett.* **2016**, *7*, 1939–1944.
- [12] Y. Takeda, R. Kanno, M. Sakano, O. Yamamoto, M. Takano, Y. Bando, H. Akinaga, K. Takita, J. B. Goodenough, *Mater. Res. Bull.* **1990**, *25*, 293–306.
- [13] C. J. Liu, M. D. Mays, D. O. Cowan, M. G. Sánchez, *Chem. Mater.* **1991**, *3*, 495–500.
- [14] R. J. Cava, B. Batlogg, T. T. Palstra, J. J. Krajewski, W. F. Peck Jr., A. P. Ramirez, L. W. Rupp Jr., *Phys. Rev. B* **1991**, *43*, 1229–1232.
- [15] J. P. Tang, R. I. Dass, A. Manthiram, *Mater. Res. Bull.* **2000**, *35*, 411–424.
- [16] T. Nitadori, M. Muramatsu, M. Misono, *Bull. Chem. Soc. Jpn.* **1988**, *61*, 3831–3837.
- [17] X. Granados, J. Fontcuberta, M. Vallet-Regí, M. J. Sayagués, J. M. González-Calbet, *J. Solid State Chem.* **1993**, *102*, 455–464.
- [18] J. Gopalakrishnan, G. Colsmann, B. Reuter, *J. Solid State Chem.* **1977**, *22*, 145–149.
- [19] I. E. Kononyuk, N. G. Surmach, L. V. Makhnach, *Inorg. Mater.* **1982**, *18*, 1029–1031.
- [20] K. Sreedhar, C. N. R. Rao, *Mater. Res. Bull.* **1990**, *25*, 1235–1242.
- [21] V. V. Vashook, S. P. Tolochko, I. I. Yushkevich, L. V. Makhnach, I. F. Kononyuk, H. Altenburg, J. Hauck, H. Ullmann, *Solid State Ionics* **1998**, *110*, 245–253.
- [22] V. V. Vashook, I. I. Yushkevich, L. V. Kokhanovsky, L. V. Makhnach, S. P. Tolochko, I. F. Kononyuk, H. Ullmann, H. Altenburg, *Solid State Ionics* **1999**, *119*, 23–30.
- [23] J. E. Millburn, M. A. Green, D. A. Neumann, M. J. Rosseinsky, *J. Solid State Chem.* **1999**, *145*, 401–420.
- [24] S. J. Skinner, J. A. Kilner, *Solid State Ionics* **2000**, *135*, 709–712.
- [25] A. Aguadero, M. J. Escudero, M. Pérez, J. A. Alonso, V. Pomjakushin, L. Daza, *Dalton Trans.* **2006**, 4377–4383.
- [26] T. Nakamura, K. Yashiro, K. Sato, J. Mizusaki, *Solid State Ionics* **2009**, *180*, 368–376.
- [27] T. Nakamura, K. Yashiro, K. Sato, J. Mizusaki, *Solid State Ionics* **2010**, *181*, 292–299.

- [28] T. Inprasit, P. Limthongkul, S. Wongkasemjit, *J. Electrochem. Soc.* **2010**, *157*, B1726–B1730.
- [29] J. Rynkowski, P. Samulkiewicz, A. K. Ladavos, P. J. Pomonis, *Appl. Catal. A* **2004**, *263*, 1–9.
- [30] A. Boreave, H. Tan, V. Roche, P. Vernoux, J. P. Deloume, *Solid State Ionics* **2008**, *179*, 1071–1075.
- [31] A. K. Ladavos, P. J. Pomonis, *Appl. Catal. A* **1997**, *165*, 73–85.
- [32] Z. Zhao, X. Yang, Y. Wu, *Appl. Catal. B* **1996**, *8*, 281–297.
- [33] K. L. Pan, S. J. Yu, S. Y. Yan, M. B. Chang, *J. Air Waste Manage. Assoc.* **2014**, *64*, 1260–1269.
- [34] R. N. Singh, T. Sharma, A. Singh, *J. New Mater. Electrochem. Syst.* **2007**, *10*, 105–111.
- [35] V. L. E. Simonsen, L. Nørskov, A. Hagen, K. K. Hansen, *J. Solid State Electrochem.* **2009**, *13*, 1529–1534.
- [36] M. Schroeder, M. A. Dragan, *J. Mater. Sci.* **2007**, *42*, 1972–1983.
- [37] Z. Li, R. Haugsrud, J. B. Smith, T. Norby, *J. Electrochem. Soc.* **2009**, *156*, B1039–B1044.
- [38] R. N. Singh, T. Sharma, A. Singh, Anindita, D. Mishra, S. K. Tiwari, *Electrochim. Acta* **2008**, *53*, 2322–2330.
- [39] R. N. Singh, A. Singh, D. Mishra, Anindita, P. Chartier, *J. Power Sources* **2008**, *185*, 776–783.
- [40] M. Gong, L. Lu, H. Zhang, L. Gao, Y. Guo, J. Jin, *Mater. Res. Bull.* **2009**, *44*, 1630–1634.
- [41] K. Kammer, *Ionics* **2009**, *15*, 325–328.
- [42] Y. Shen, H. Zhao, J. Xu, X. Zhang, K. Zheng, K. Świerczek, *Int. J. Hydrogen Energy* **2014**, *39*, 1023–1029.
- [43] E. Yu. Pikalova, N. M. Bogdanovich, A. A. Kolchugin, D. A. Osinkin, D. I. Bronin, *Proc. Eng.* **2014**, *98*, 105–110.
- [44] B. Guan, W. Li, H. Zhang, X. Liu, *J. Electrochem. Soc.* **2015**, *162*, F707–F712.
- [45] Y. P. Wang, Q. Xu, D. P. Huang, K. Zhao, M. Chen, B. H. Kim, *Int. J. Hydrogen Energy* **2016**, *41*, 6476–6485.
- [46] L. V. Makhnach, S. P. Tolochko, I. F. Kononyuk, V. V. Vashuk, S. A. Prodan, *Inorg. Mater.* **1993**, *29*, 1509–1513.
- [47] L. V. Makhnach, V. V. Pankov, P. Strobel, *Mater. Chem. Phys.* **2008**, *111*, 125–130.
- [48] E. Kravchenko, K. Zakharchuk, A. Viskup, J. Grins, G. Svensson, V. Pankov, A. Yaremchenko, *ChemSusChem* **2017**, *10*, 600–611.
- [49] E. Kravchenko, D. Khalyavin, K. Zakharchuk, J. Grins, G. Svensson, V. Pankov, A. Yaremchenko, *J. Mater. Chem. A* **2015**, *3*, 23852–23863.
- [50] A. Manthiram, J. P. Tang, V. Manivannan, *J. Solid State Chem.* **1999**, *148*, 499–507.
- [51] M. Crespin, J. M. Bassat, P. Odier, P. Mouron, J. Choisnet, *J. Solid State Chem.* **1990**, *84*, 165–170.
- [52] M. Crespin, C. Landron, P. Odier, J. M. Bassat, P. Mouron, J. Choisnet, *J. Solid State Chem.* **1992**, *100*, 281–291.
- [53] M. Medarde, J. Rodríguez-Carvajal, X. Obradors, M. Vallet-Regí, J. M. González-Calbet, M. J. Sayagués, *Phys. B* **1992**, *180–181*, 399–401.
- [54] C. L. Teske, H. Müller-Buschbaum, *Z. Anorg. Allg. Chem.* **1969**, *371*, 325–332.
- [55] M. T. Weller, D. R. Lines, *J. Solid State Chem.* **1989**, *82*, 21–29.
- [56] J. C. Barry, *J. Electron Microsc. Technol.* **1988**, *8*, 325–337.
- [57] S. Amelinckx, G. Vantendelo, J. Vanlanduyt, *Solid State Ionics* **1990**, *39*, 37–47.
- [58] G. Van Tendeloo, H. W. Zandbergen, J. Van Landuyt, S. Amelinckx, *Mater. Charact.* **1997**, *39*, 599–629.
- [59] D. Marrocchelli, S. R. Bishop, H. L. Tuller, B. Yildiz, *Adv. Funct. Mater.* **2012**, *22*, 1958–1965.
- [60] D. Marrocchelli, N. H. Perry, S. R. Bishop, *Phys. Chem. Chem. Phys.* **2015**, *17*, 10028–10039.
- [61] J. R. Frade in *Solid Oxide Fuels Cells: Facts and Figures* (Eds.: J. T. S. Irvine, P. Connor), Springer-Verlag, London, **2013**, pp. 95–119.
- [62] A. A. Yaremchenko, S. M. Mikhalev, E. S. Kravchenko, J. R. Frade, *J. Eur. Ceram. Soc.* **2014**, *34*, 703–715.
- [63] V. V. Vashook, N. E. Trofimenko, H. Ullmann, L. V. Makhnach, *Solid State Ionics* **2000**, *131*, 329–336.
- [64] A. C. Tomkiewicz, M. Tamimi, A. Huq, S. McIntosh, *J. Mater. Chem. A* **2015**, *3*, 21864–21874.
- [65] T. L. Meyer, L. Jiang, J. Lee, M. Yoon, J. W. Freeland, J. H. Jang, D. S. Aidhy, A. Borisevich, M. Chisholm, T. Egami, H. N. Lee, *eprint arXiv* **2015**, *1508*, 06971, <http://arxiv.org/abs/1508.06971> (accessed January 2018).
- [66] R. D. Shannon, *Acta Crystallogr., Sect. A* **1976**, *32*, 751–767.
- [67] V. V. Kharton, A. V. Kovalevsky, M. Avdeev, E. V. Tsipis, M. V. Patrakeev, A. A. Yaremchenko, E. N. Naumovich, J. R. Frade, *Chem. Mater.* **2007**, *19*, 2027–2033.
- [68] T. Nakamura, Y. Ling, K. Amezawa, *J. Mater. Chem. A* **2015**, *3*, 10471–10479.
- [69] H. Kanai, T. Hashimoto, H. Tagawa, J. Mizusaki, *Electrochemistry* **2000**, *68*, 507–514.
- [70] M. Ohtani, H. Kishida, K. Hirota, H. Sakurada, N. Kawamoto, Y. Murakami, K. Ueno, J. Matsuno, Y. Okimoto, T. Makino, Y. Segawa, Y. Tokura, D. Shindo, H. Okamoto, M. Kawasaki, *Adv. Mater.* **2006**, *18*, 2541–2544.
- [71] H. Gui, X. Li, Z. Zhao, W. Xie, *Mod. Phys. Lett. B* **2016**, *30*, 1650119.

Received: January 21, 2018